JOURNAL OF MATERIALS SCIENCE 28 (1993) 5280–5296

Debond coating requirements for brittle matrix composites

M.L. EMILIANI
Pratt and Whitney, Materials Engineering, P.O. Box 109600, Mail Stop 706-06, West Palm Beach, FL 33410, USA

The cause of improved fracture toughness in Y_2O_3-coated niobium-toughened TiAl relative to either uncoated niobium or Al_2O_3-coated niobium was examined. Reactively sputtered Y_2O_3 coatings, 1–2 μm thick, were deposited on to rock salt (NaCl), polished single-crystal (0 0 0 1) Al_2O_3, and polished polycrystalline niobium. Sputtered niobium coatings, 1–2 μm thick, were also deposited on to polished single-crystal Y_2O_3 substrates for comparison. The oxide coating was characterized and consisted of stoichiometric b c c Y_2O_3 with $a_0 = 1.0602$ nm. Indentation tests were performed to correlate the fracture toughness and debond characteristics of as-deposited Y_2O_3 coatings on Al_2O_3 and polycrystalline niobium, and niobium coatings on single-crystal Y_2O_3, to that found in TiAl/Nb and Al_2O_3/Al_2O_3 laminates. The calculated fracture toughness of sputtered Y_2O_3 on sapphire was similar to reported values for bulk Y_2O_3. However, a wide variation in interfacial fracture toughness was obtained by indentation methods, and is attributed to the microstructure of as-deposited coatings and to weak bonding between as-deposited yttria and the sapphire substrate. These results are related to factors that affect debonding and fracture toughness of brittle matrix composites. Reactive and non-reactive metal/ceramic systems were reviewed in an effort to understand why Y_2O_3 coatings perform well. It is postulated that yttrium oxide coatings applied to niobium have an atomically sharp interface that has a lower fracture energy compared to Nb/Al_2O_3, resulting in improved interfacial debonding and composite fracture toughness.

1. Introduction

Fibre coatings will probably be required for brittle matrix composites in order to improve composite fracture toughness or reduce fibre/matrix interaction at elevated temperatures [1–4]. Coatings have been successfully used to improve the thermochemical compatibility or fracture behaviour of a few ductile and brittle matrix systems including boron- [4] or SiC- [5] reinforced titanium or aluminium alloys and SiC-reinforced lithium aluminosilicate (AS) glass [2]. The purpose of this research was to identify protective and debond coatings that improve the toughness of intermetallic and ceramic matrix composites, and contribute to a generalized understanding of the requirements for successful debond coatings. The latter may allow the development of predictive guidelines for future coating selections in other composite systems.

Two composite systems, niobium-reinforced TiAl and Al_2O_3-reinforced Al_2O_3, have exhibited improved fracture toughness through the use of chemically compatible interfacial coatings [6, 7]. An elastic indentation technique, Hertzian cone cracking, has been used to assess the specific fracture energy, Γ_i, of Al_2O_3 laminate composites containing various interfacial coatings [7]. Yttria interfacial coatings, applied by sputtering or sol–gel, exhibit a specific fracture energy of 25 J m^{-2}. This is approximately five times greater than that achieved with sputtered molybdenum coatings [8], and results in incomplete debonding. Reaction between the Al_2O_3 substrate and Y_2O_3 to form YAG ($Y_3Al_5O_{12}$) was found to be responsible for the high fracture energy.

The debonding characteristics of a model niobium-reinforced TiAl composite have been evaluated using uncoated niobium, Al_2O_3-coated niobium, and Y_2O_3-coated niobium [6]. Uniaxial tension tests of pre-cracked TiAl/Nb laminates were performed *in situ* in the scanning electron microscope. The Y_2O_3 coating produced the lowest specific fracture energy, thus allowing extensive debonding which permitted plastic deformation of the niobium over a large volume and resulting in a high work of rupture. The measured fracture toughness is thought to be due to the presence of an atomically sharp Y_2O_3/Nb interface similar to that found in Al_2O_3/Nb couples [9].

The present study examines as-sputtered Y_2O_3 coatings deposited on to rock salt (NaCl), single-crystal (0 0 0 1) Al_2O_3, and polycrystalline niobium to understand better why this coating improves the toughness of niobium-reinforced TiAl. As-deposited yttria coatings were characterized by scanning electron microscopy (SEM), energy dispersive spectroscopy (EDS), transmission electron microscopy (TEM), X-ray photoelectron spectroscopy (XPS),

secondary ion mass spectroscopy (SIMS), X-ray diffraction (XRD), and indentation techniques. Nanoindenter® and Vickers indentation tests [10] were used to determine the fracture toughness, K_c, interfacial fracture toughness $K_{c,i}$, and specific fracture energy, Γ_i, of as-sputtered coatings. The results were compared to that found for diffusion-bonded Al_2O_3/Al_2O_3 and TiAl/Nb laminates [6, 7]. In addition, niobium coatings, 1–2 μm thick, were deposited on to polished single-crystal Y_2O_3 wafers by sputtering to compare debonding behaviour. A TEM study was also performed on Y_2O_3-coated niobium-reinforced TiAl laminate.

2. Experimental procedure

2.1. Sputtered coatings

Yttrium oxide coatings were deposited on to polished single-crystal Al_2O_3 4 mm thick, commercial purity polycrystalline niobium foil 125 μm thick, and rock salt substrates. Prior to coating, Al_2O_3 and niobium substrates were ultrasonically cleaned in soapy water, rinsed in water, rinsed in ethyl alcohol, and dried by forced hot air. Sputtering was performed in a Plasma-Therm Model AMNS-1000E 1000 W radio frequency diode sputtering unit equipped with dual-opposed 6 in ($\sim$15.24 cm) diameter yttrium metal targets (99.9 wt % purity). A 142 μm monofilament SiC fibre (Textron SCS-6) was also coated to determine coating thickness and microstructure by fractography. Yttrium oxide coatings were deposited by reactive sputtering using a 50%–50% mixture of research grade argon and oxygen at a total working gas pressure of $P_T = 6$ m torr. The substrates were not externally cooled, heated, or biased during sputtering. The top and bottom targets were maintained at 3000 and 500 V, respectively. Deposition of Y_2O_3 for $\sim$10 h resulted in coatings 1–2 μm thick. The only equilibrium oxide phase formed according to the Y–O phase diagram is Y_2O_3 [11].

Niobium coatings were sputter deposited on to polished Y_2O_3 wafers $\sim$0.5 mm thick using research-grade argon at $P_T = 6$ m torr and 99.5 wt % purity niobium metal targets maintained at 5000 and 500 V. The resultant coatings were 3–4 μm thick.

2.2. Indentation tests to determine coating hardness and elastic modulus

The hardness and elastic modulus of as-sputtered coatings were determined using a Nano Instruments Inc. Nanoindenter® [12]. This instrument is a submicrometre indentation tester that uses a triangular diamond indentor with the same projected area-to-depth ratio as the Vickers square pyramid indentor. The maximum load that can be applied by this technique is 0.1 N. Coating hardness and modulus were determined by taking five or more indentations at depths ranging from 0.04–0.7 μm.

2.3. Indentation tests to determine coating fracture properties

Nanoindenter® and Vickers indentation tests were used to initiate coating fracture or interfacial debonding in Y_2O_3-coated Al_2O_3, Y_2O_3-coated niobium and niobium coated Y_2O_3. All coatings were evaluated in the as-sputtered condition. Loads greater than 0.1 N and up to 10 N were applied using a Vickers diamond indentor. Six measurements are typically made at each indentation depth. While there are numerous relationships for obtaining quantitative values of fracture toughness [13], only selected equations are applied in the present study. The equations used to determine coating fracture toughness, K_c, interfacial fracture toughness, $K_{c,i}$, and specific fracture energy, Γ_i are briefly reviewed.

The fracture toughness of thin coatings can be determined by measuring radial crack lengths and the dimensions of indentations made by indentation tests [13, 14]. Equations to determine fracture toughness have been empirically determined assuming the crack shape is radial–median (i.e. "halfpenny") or Palmqvist

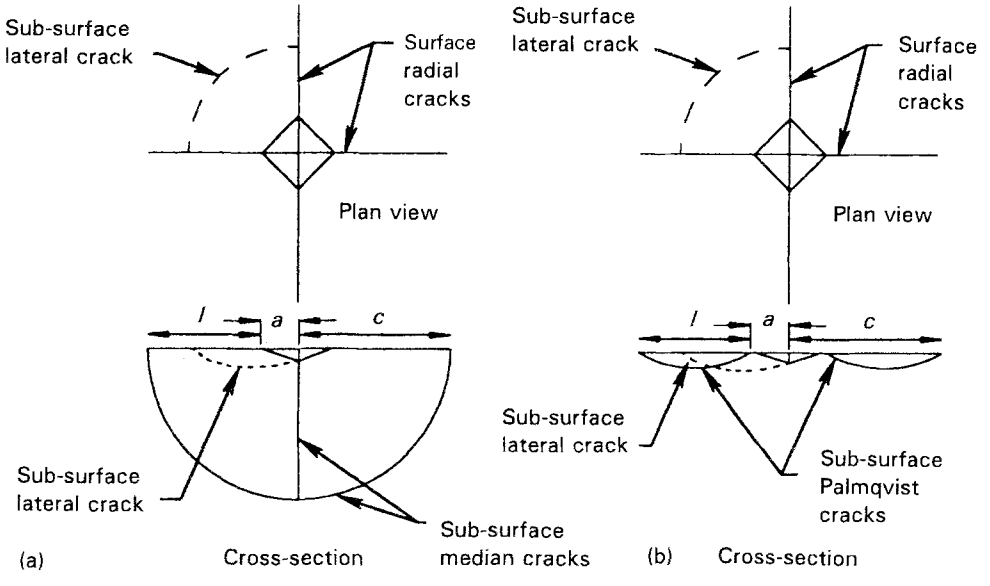

Figure 1 Schematic diagrams of Vickers indentations resulting in the formation of (a) radial–median and (b) Palmqvist cracks [14].

[14]. The critical indentation and crack-related dimensions are the indentation half-diagonal length, a, radial surface crack length, C, and the Palmqvist surface crack length, l (Fig. 1). Equations to determine fracture toughness take the following general form for halfpenny (Equation 1) and Palmqvist (Equation 2) shaped cracks [14]

$$K_c = k\frac{P}{aC^{1/2}} \quad (1)$$

$$K_c = k\,(E/H_v)^{2/5}\frac{P}{al^{1/2}} \quad (2)$$

where k is a constant typically between 0.001 and 0.5, P is the applied indentor load (N), H_v is the Vickers microhardness (GPa), E is the elastic modulus (GPa), and a, C, l are the indentation and crack related-dimensions (m), as shown in Fig. 1. Values of K_c for selected glass and oxide ceramics have been compared to K_{Ic} fracture toughness of the same materials by traditional mechanical testing techniques [13]. The average results for both types of test were reported to be within $\pm$ 30%. Thus, the values of fracture toughness obtained by indentation methods are comparable to that obtained by more elaborate mechanical tests. In general, averaged values of fracture toughness calculated using either halfpenny or Palmqvist-based equations yield similar results.

The interfacial fracture toughness, $K_{c,i}$, of thin coatings can also be determined from indentation tests [15]. This information also provides a measure of coating adhesion to the substrate, and is required to determine the specific fracture energy, Γ_i, of the interface. The interfacial fracture toughness can be represented by

$$K_{c,i} = k\,t^{3/2}H_v^{1/2}\frac{(1 - P_0/P)P^{1/2}}{C^2} \quad (3)$$

where k is a constant determined to be 0.16 in the present study, t is the coating thickness (m), H_v is the Vickers hardness of the coating (GPa), P_0 is the threshold load for crack formation (MN), P is the maximum indentor load (MN), and C is the lateral crack length (m). Knowledge of the fracture toughness allows calculation of the specific fracture energy, Γ_i, and provides a basis for understanding the contribution of coatings to interfacial debonding. The fracture toughness for a Mode I (tensile) crack is [16]

$$K_{Ic} = Y\,\sigma\,(\pi a^{1/2}) \quad (4)$$

where Y is the geometric crack factor (typically $= \pi^{1/2}$ for a halfpenny-shaped crack), σ is the applied stress (N), and a is the half-crack length (m). The Griffith relationship for plane (biaxial) stress ($\sigma_Z = 0$) is

$$\sigma = (2\,E\,\gamma_s/\pi\,a)^{1/2} \quad (5)$$

Combining Equations 4 and 5 yields the specific fracture energy

$$\gamma_s = \frac{K_{Ic}^2}{2\,Y\,E} = \Gamma_i \quad (6)$$

Thus, the specific fracture energy (in J m^{-2}), depends only upon the fracture toughness (where $K_{Ic} = K_c$ or $K_{c,i}$), geometric crack factor, and elastic modulus of the coating. The latter may vary depending upon thickness.

3. Results

3.1. Characterization of sputtered Y_2O_3 coatings

X-ray diffraction of yttria-coated sapphire wafer was performed using a Huber Model 651 Guinier thin-film goniometer. The resulting spectrum corresponds to bcc Y_2O_3 (JCPDS pattern 25-1200), Fig. 2. X-ray

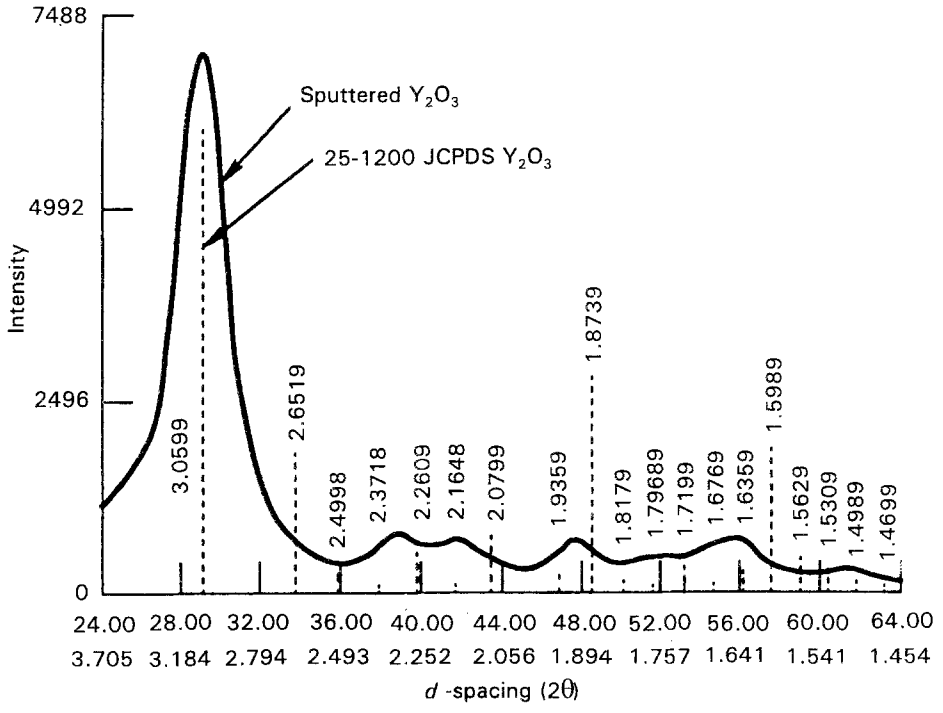

Figure 2 X-ray diffraction pattern of reactively sputtered Y_2O_3 showing good correlation with the JCPDS reference pattern (vertical lines).

photoelectron spectroscopy was performed using a PHI Model 5400 multiprobe. The surface contained excess physisorbed hydrocarbon or carbon and oxygen or oxide due to exposure to the ambient. Oxygen in the form of OH or H_2O was detected. Argon sputtering to a depth of ~ 5 nm removed gross contaminants, resulting in decreased carbon and increased oxygen signals. Additional sputtering to a depth of 10 nm showed only yttrium and oxygen (Fig. 3). Secondary ion mass spectroscopy (SIMS) data were obtained using a Kratos Ion Microprobe. SIMS showed that boron, carbon, aluminium, silicon, potassium, titanium, iron, niobium and neodymium were present in the coating ~ 10 nm below the free surface, all at levels of < 0.1 at %.

The surface finish of Y_2O_3 coatings on SiC fibres was examined by SEM and found faithfully to replicate the surface finish of the substrate which consists of nodules characteristic of coatings deposited by chemical vapour deposition (Fig. 4). Coating microstructure was characterized by SEM of fractured SiC fibres and found to consist of columnar grains which extend through the thickness of the coating. This is typical of that found in sputtered coatings deposited at low homologous temperature (T/T_M, where T is the substrate temperature and T_M the melting temperature of Y_2O_3) [17, 18]. For $T_M(Y_2O_3) = 2400\,^{\circ}C$ and assuming $T_{substrate} \approx 300\,^{\circ}C$, $T/T_M \approx 0.12$. These coatings were found to correspond well to the Zone 1 microstructure as described by Thornton [18].

Electron-transparent Y_2O_3 samples for TEM were produced by depositing a thin coating on to rock salt, dissolving the substrate in water, then collecting the oxide film on a copper grid. Y_2O_3 samples were

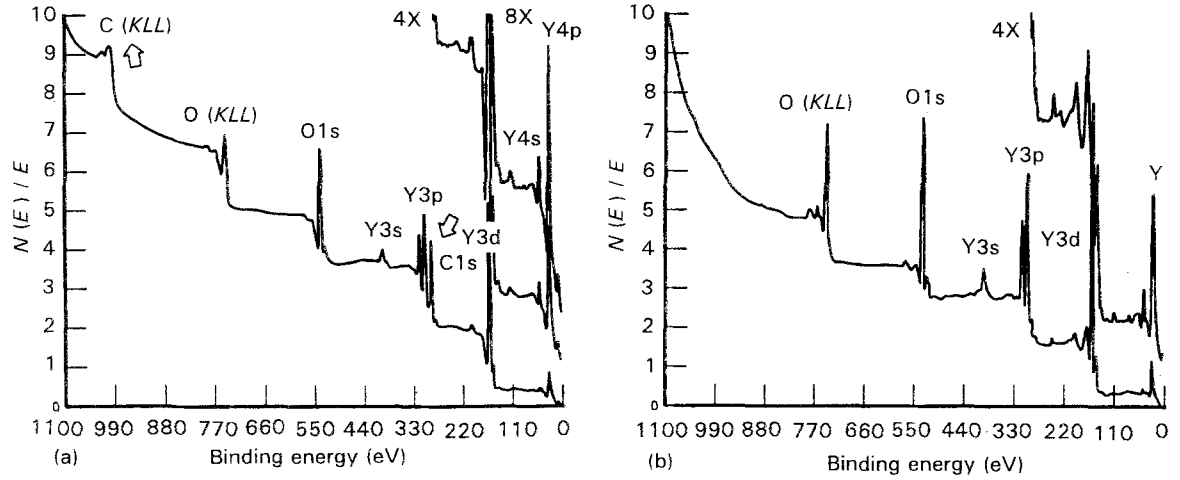

Figure 3 XPS spectra of Y_2O_3 coating, (a) as-received, and (b) 10 nm below the free surface. The carbon signal is prominent in as-received samples (arrowed), while only yttrium and oxygen are present 10 nm below the free surface.

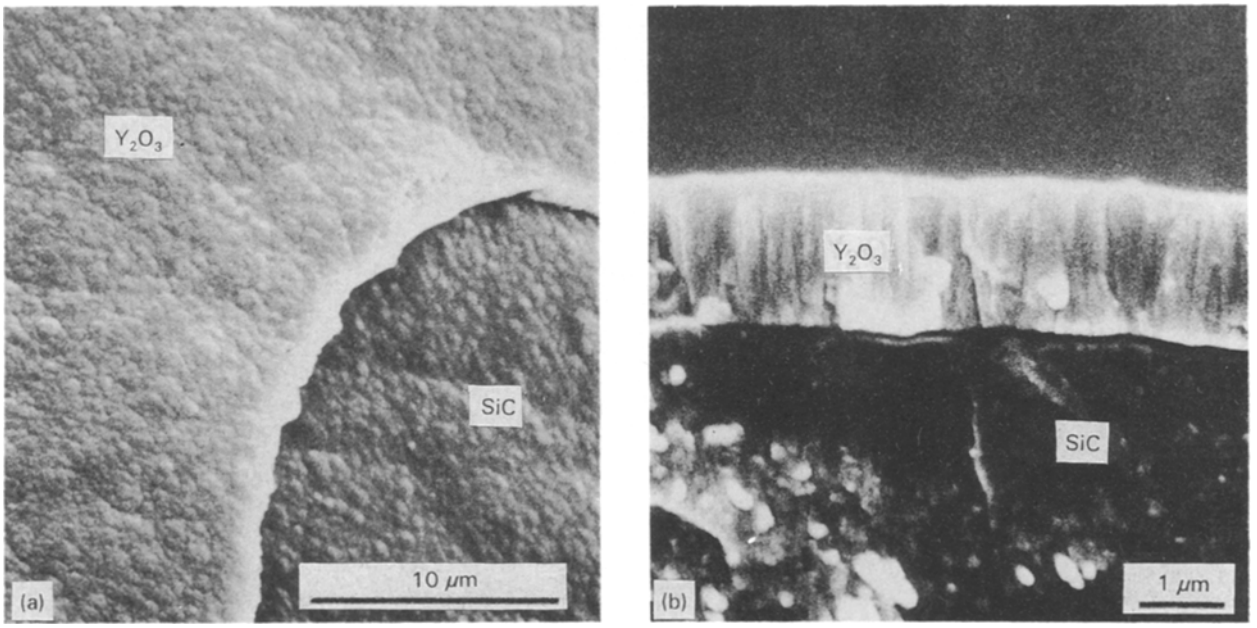

Figure 4 (a) Scanning electron micrograph showing the surface finish of as-deposited Y_2O_3 coating which has replicated the surface finish of the SiC fibre. (b) Scanning electron micrograph showing the thickness and structure of as-deposited Y_2O_3 coating. The columnar morphology of the coating is evident.

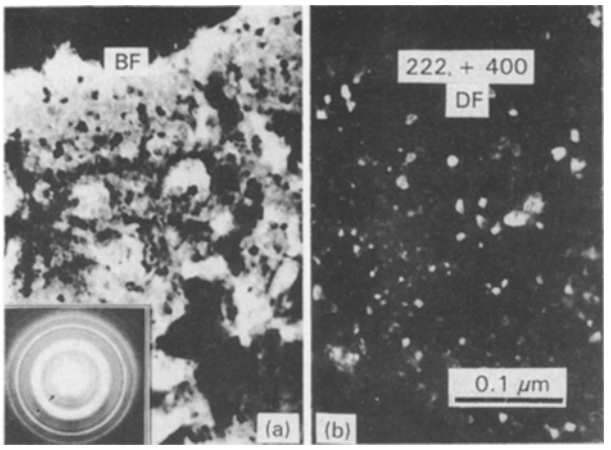

Figure 5 (a) Bright-field (BF) and (b) dark-field (DF) transmission electron micrographs of as-sputtered Y_2O_3. Arrows on the selected-area diffraction pattern (inset) bracket the two rings used to make the dark-field micrograph. The coating consists of bcc Y_2O_3 with $a_0 = 1.0602$ nm.

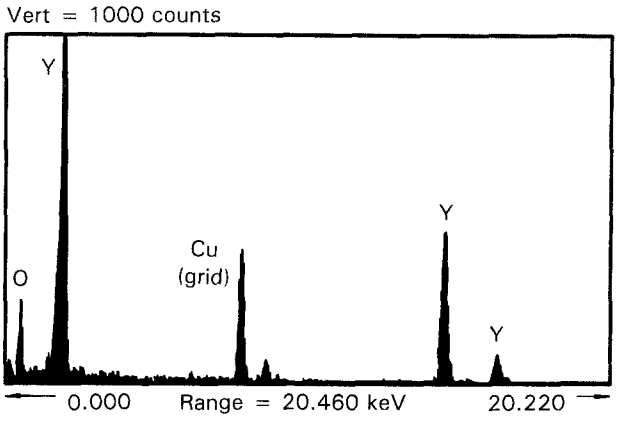

Figure 6 Energy-dispersive X-ray spectrum of the Y_2O_3 coating.

examined using a Philips 400T at 120 kV and equipped with a Kevex Quantum energy-dispersive X-ray spectrometer. Direct imaging of the coating microstructure through-thickness by transmission electron microscopy showed it contained a homogeneous distribution of fine grains 10–30 nm diameter (Fig. 5). Energy dispersive spectroscopy of the coating showed yttrium and oxygen (Fig. 6). Selected-area electron diffraction patterns (Fig. 5, inset) contained well-defined continuous rings with spacings characteristic of body-centred cubic Y_2O_3 (Pearson Symbol cI80, Mn_2O_3 prototype structure), with a lattice parameter of $a_0 = 1.0602$ nm.

Yttrium oxide-coated niobium foils were diffusion bonded between two TiAl plates in vacuum at 1066 °C under a pressure of 10 MPa for 4 h (Fig. 7) [6]. The resulting laminate was prepared for TEM by sectioning small wafers perpendicular to the TiAl/Y_2O_3/Nb interface using a low-speed diamond saw. Most of the samples fractured during sectioning, grinding to final thickness, or ion milling due to the low specific fracture energy of the Y_2O_3/Nb interface.

The interface between Y_2O_3 and niobium is of interest because it is the location where debonding

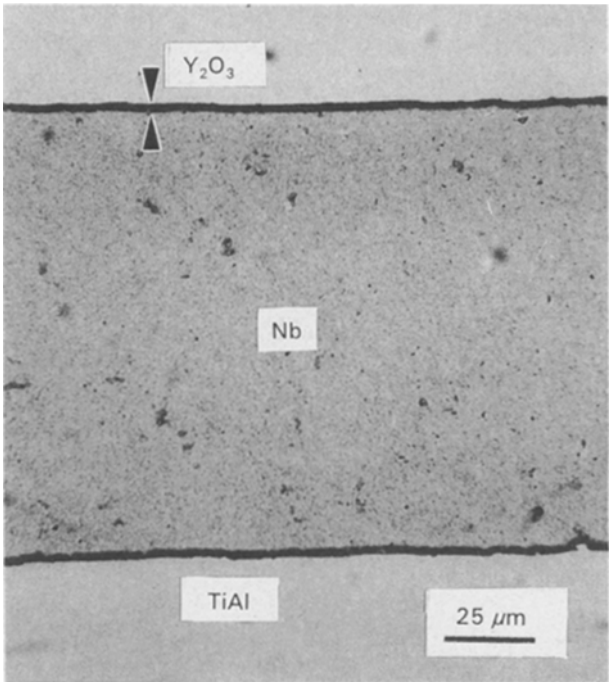

Figure 7 Light micrograph of a TiAl/Nb laminate test specimen after diffusion bonding at 1066 °C for 4 h and 10 MPa pressure. Note the absence of interfacial reaction products.

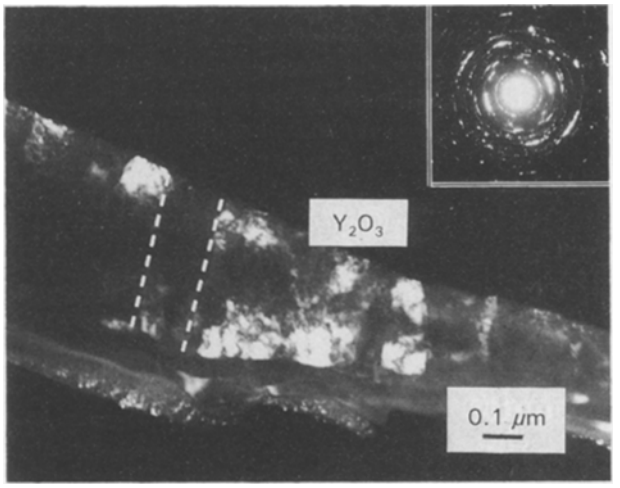

Figure 8 Transmission electron micrograph of a portion of the Y_2O_3 coating and selected-area electron diffraction pattern (inset) from a TiAl/Nb laminate. Note the grains remain columnar after hot-pressing at 1066 °C for 4 h.

occurs. Unfortunately, it could not be observed due to decohesion of the interface. The Y_2O_3/TiAl interface is more strongly bonded and therefore could be examined by TEM. The most interesting aspect of this interface is the morphology of Y_2O_3 coating (Fig. 8), which has been exposed to 1066 °C for 4 h. The Y_2O_3 coating retains a columnar morphology, with columns ~0.15 μm wide and extending through the entire thickness of the coating. Reflections from selected-area diffraction patterns contained intense arcs. This, coupled with the shape of individual grains, suggests that the columnar Y_2O_3 grains contain a dense substructure of low-angle grain boundaries that have begun to coalesce. Thus, diffusion bonding resulted in

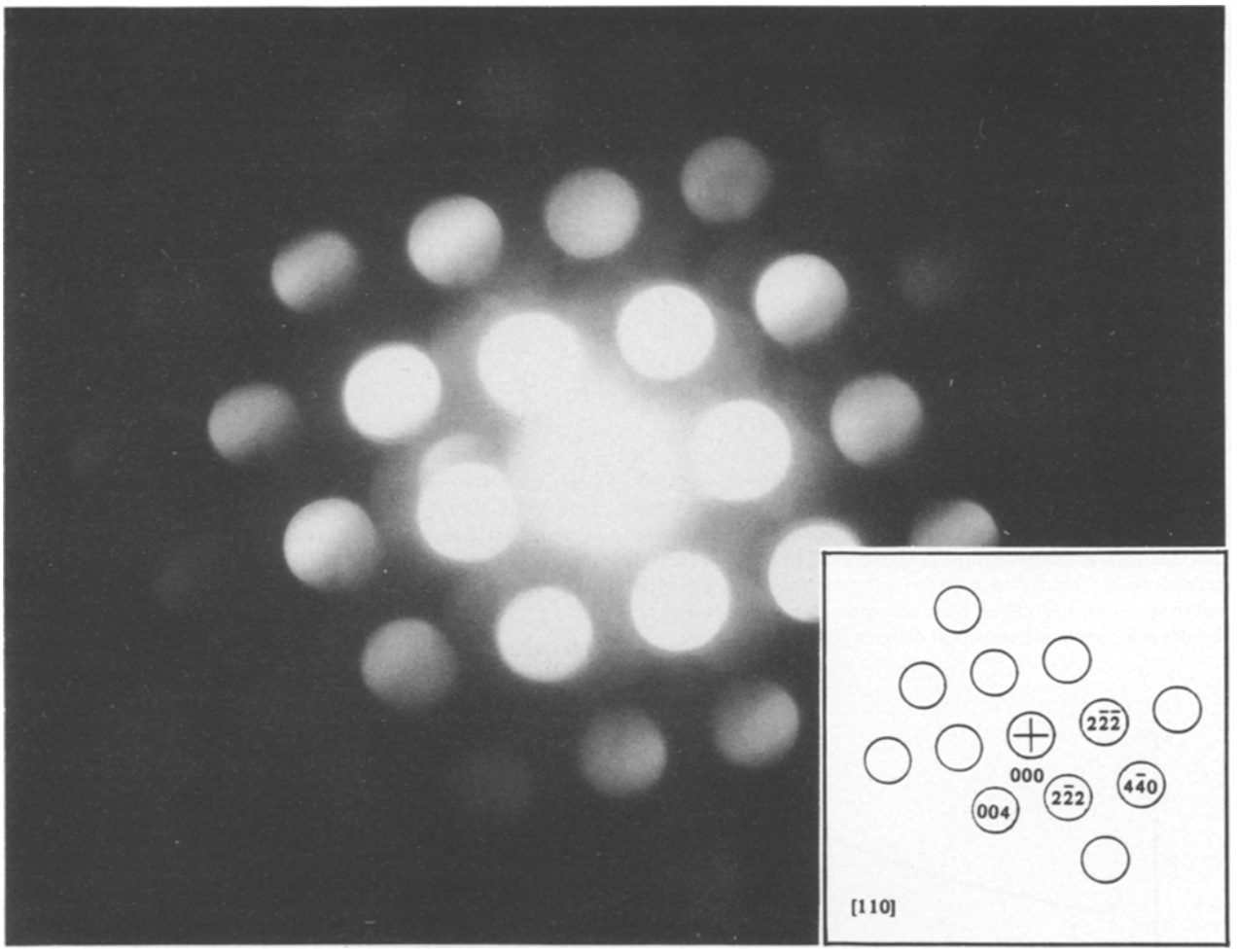

Figure 9 Convergent-beam electron diffraction pattern of Y_2O_3 and corresponding computer-generated [1 1 0] zone axis pattern.

little or no grain growth of the oxide coating. Selected-area (Fig. 8, inset) and convergent beam electron diffraction (Fig. 9) of the coating shows it consists of cubic Y_2O_3 with lattice parameter of $a_0 = 1.0602$ nm, and is in agreement with the results for as-deposited Y_2O_3. Direct imaging and EDS did not reveal extensive chemical reaction between Y_2O_3 and TiAl.

3.2. Indentation-derived coating hardness and elastic modulus

The hardness of as-sputtered yttria coatings on polished sapphire substrates was determined using the Nanoindenter® by taking five or more indentations at depths ranging from 0.05–0.5 μm. Fig. 10 shows the variation in coating hardness as a function of indentation depth. The rapid increase in hardness with decreasing indentation depth is due to the well-known indentation size effect [19]. However, at indentation depths ≥ 0.4 μm the hardness remains nearly constant at ~ 750 kg mm^{-2} (7.5 GPa). This is in good agreement with previous results for bulk Y_2O_3 [20].

The hardness of as-sputtered Y_2O_3 coating on commercially pure polycrystalline niobium was also determined using the Nanoindenter® (Fig. 11). There is a dramatic decrease at ~ 0.6 μm depth due to plastic deformation of the soft niobium substrate (film–substrate effect, FSE) [21]. Conversely, a rapid increase in hardness was found at indentation depths

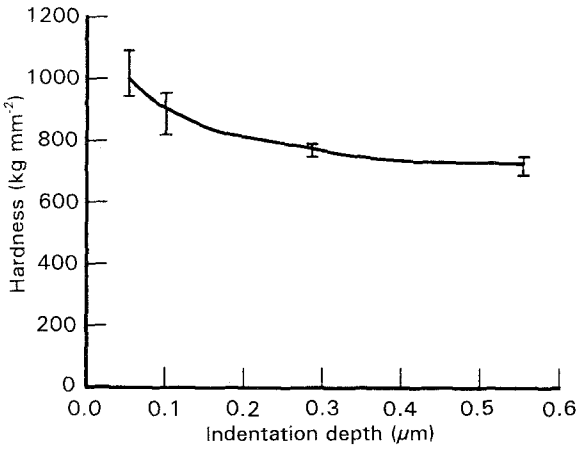

Figure 10 Hardness versus indentation depth as determined by the nanoindentation technique. The hardeness of Y_2O_3 at ~ 0.5 μm deep indentations is ~ 750 kg mm^{-2} (7.5 GPa). Higher hardness at smaller indentation depths are due to the indentation size effect [19].

< 0.1 μm due to the indentation size effect (ISE) [19]. The hardness of the Y_2O_3 coating measured at indentation depths between $0.1\ \mu m < d < 0.5\ \mu m$ is 800–850 kg mm^{-2} (8–8.5 GPa). This is approximately the same hardness as that measured for as-sputtered Y_2O_3 on single-crystal Al_2O_3, and agrees with that reported for bulk Y_2O_3 [20, 22]. Thus, accurate values of Y_2O_3 coating hardness independent of the sub-

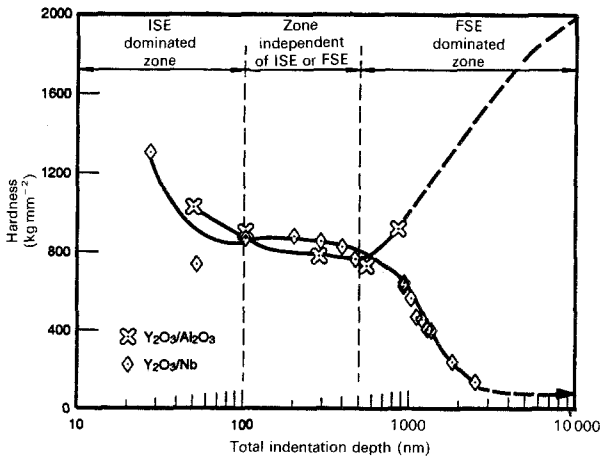

Figure 11 Plot of Nanoindenter® hardness versus indentation depth for as-sputtered Y_2O_3 coating on Al_2O_3 and niobium. High hardness values are obtained at indentation depths < 0.1 μm due to the indentation size effect (ISE) [14], while the coating hardness is dominated by interaction with the substrate for $d \gtrsim 0.8$ μm (film substrate effect, FSE) [21]. Note the good correlation in coating hardness for indentations depths between 0.1 and 0.5 μm.

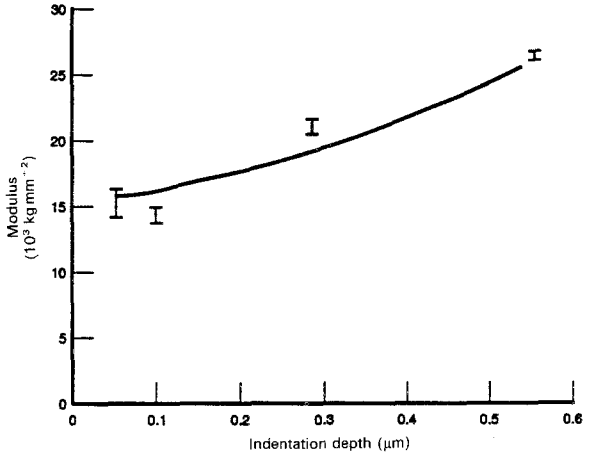

Figure 12 Elastic modulus of Y_2O_3 versus indentation depth. The modulus at small indentation depths (0.05–0.1 μm) is characteristic of bulk Y_2O_3.

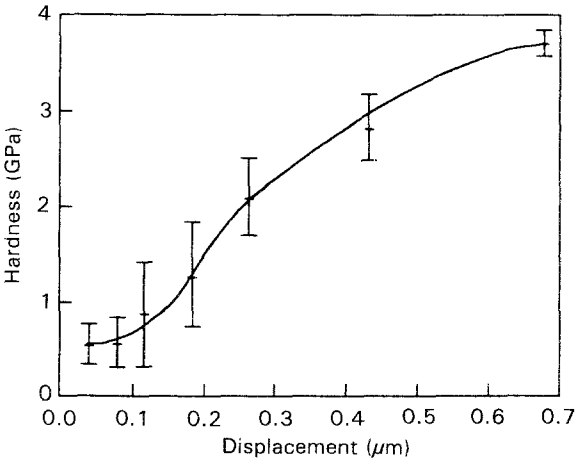

Figure 13 Hardness versus indentation depth as determined by the nanoindentation technique. The hardness of niobium at ~0.4 μm deep indentations is 2.8 GPa.

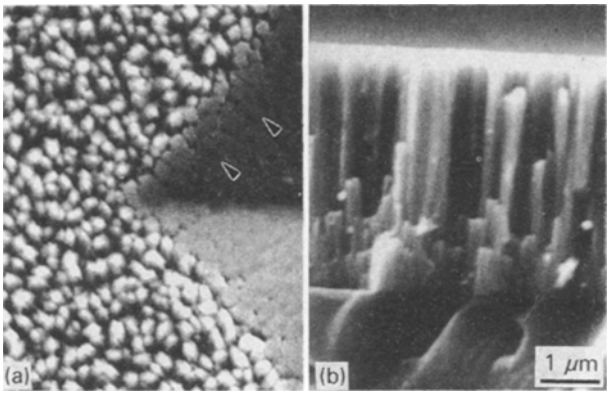

Figure 14 (a) Scanning electron micrograph showing the surface finish of as-deposited niobium coating which consists of domed tops ~0.2 μm in diameter. Note the Vickers indentation which made only partial contact with the coating at the edged (arrowed). (b) Scanning electron micrograph showing the thickness and columnar structure of as-deposited niobium.

strate material were determined using the Nanoindenter® at indentation depths between 0.1 and 0.3 μm.

The elastic modulus of Y_2O_3 coatings was also determined using the Nanoindenter® (Fig. 12), assuming Poisson's ratio = 0.33. The modulus increases almost linearly from 15×10^3–27×10^3 kg mm^{-2} (150–270 GPa) throughout the range of indentation depths. The elastic modulus of Y_2O_3 at ~0.5 μm indentation depths approaches that of bulk Al_2O_3 (~350 GPa), indicating that the coating modulus is very sensitive to substrate modulus. The elastic modulus of bulk Y_2O_3 is reported as $\sim 13.4 \times 10^3$ kg mm^{-2} (134 GPa) [23], and is in agreement with data generated at indentation depths of 0.05–0.1 μm.

The hardness and elastic modulus of niobium coatings on Y_2O_3 were determined from indentations ranging in depth from 0.04–0.7 μm. The hardness increased with increasing indentation depth due to the film–substrate effect (Fig. 13). To minimize this effect, the ratio of indentation depth to coating thickness should be $d/t < 0.1$ (Fig. 14a). However, indentations less than 0.4 μm may be influenced by surface roughness (Fig. 14b). Because of these factors, the hardness at a depth of ~ 0.4 μm, $H_v \approx 2.8$ GPa, is expected to be representative of the actual hardness of the niobium film. In contrast, the hardness of bulk wrought niobium is ~ 1.6 GPa [24]. A plot of the elastic modulus of the niobium film versus indentation depth shows less dependence upon substrate effects (Fig. 15), and $E = 88$ GPa at an indentation depth of 0.4 μm. This value is in reasonable agreement with the literature [25].

3.3. Y_2O_3 coating on sapphire

3.3.1 Coating fracture toughness, K_c

The Nanoindenter® could not be used to determine the coating fracture toughness K_c, because the maximum load was insufficient to initiate radial cracks. Vickers indentation tests were therefore used to obtain the desired crack morphology. The yttrium oxide coating spalled from alumina substrates at loads as

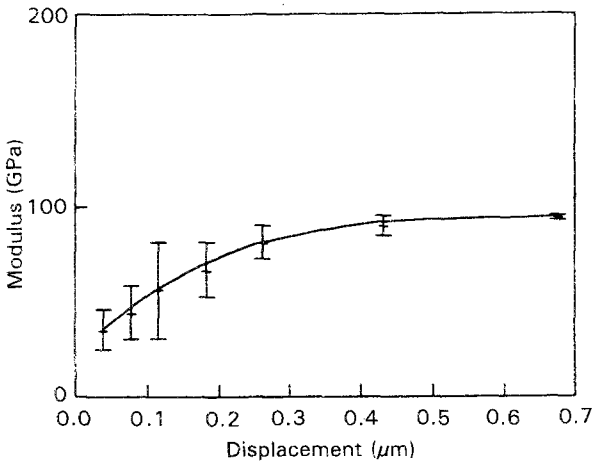

Figure 15 Elastic modulus of niobium versus indentation depth. The modulus at an indentation depth of 0.4 μm is ~88 GPa.

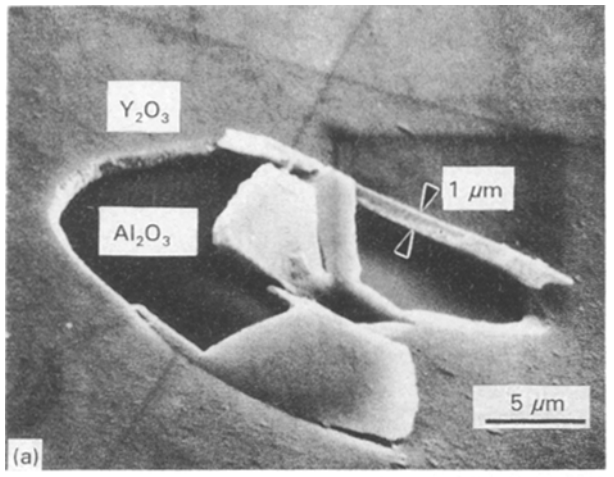

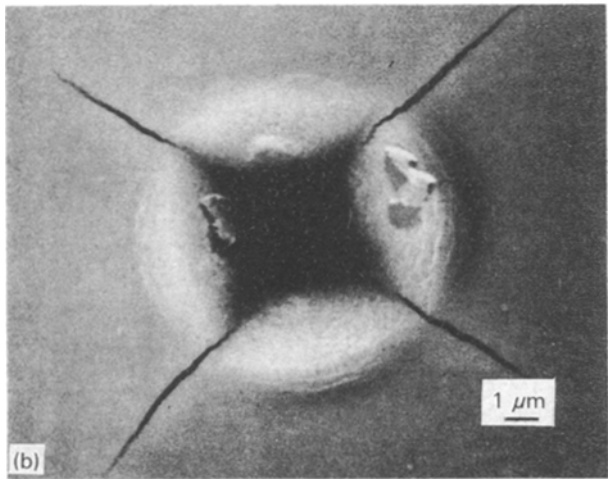

Figure 16 (a) Scanning electron micrograph of Y_2O_3 coating spalled from (0001) sapphire substrate by a 0.196 N Vickers indentation. The coating thickness is ~1 μm. (b) Backscattered scanning electron micrograph of a Vickers indentation in Y_2O_3 coating at 0.49 N load. Note the radial cracks at the corners of the indentation.

low as 0.147 N (Fig. 16a). Approximately 0.02 μm gold was sputtered on to the Y_2O_3 to prevent coating spallation and post-indentation slow crack growth. This should not effect the fracture toughness results because the gold film is < 2% of the Y_2O_3 coating thickness. Further, the hardness of the Y_2O_3 coating,

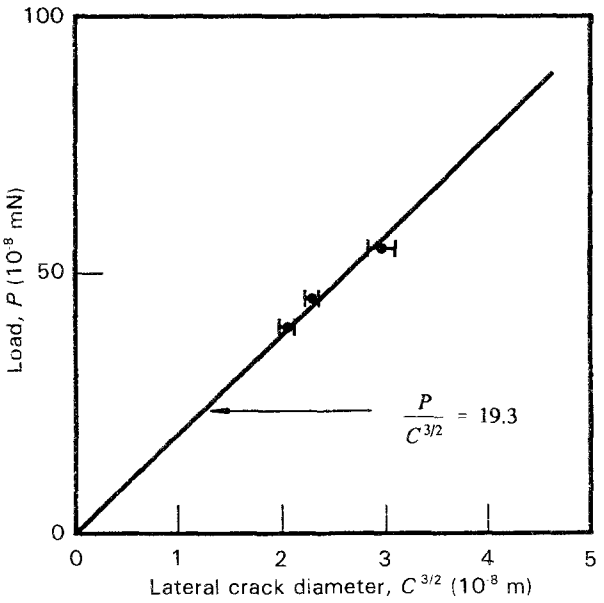

Figure 17 Plot of Vickers indentation load versus radial crack length used to determine the fracture toughness of sputtered Y_2O_3 coatings on sapphire.

as measured using the Nanoindenter®, was unaffected by the gold film.

Vickers indentation tests of gold-coated Y_2O_3 did not produce radial cracks at loads less than 0.391 N, while loads > 0.538 N caused coating spallation which prevented measurement of radial cracks. Fig. 16b shows radial cracks introduced in Y_2O_3 by Vickers indentation at 0.49 N load. Five indentations were made at various loads to obtain average values of radial crack length. The indentor load is plotted versus the radial crack length according to the relation [26].

$$K_c = 0.019\,[E/H_v]^{1/2}\frac{P}{C^{3/2}} \quad (7)$$

where E is the elastic modulus of the coating (GPa), H_v is the Vickers hardness (GPa), P the applied load (N), and C the radial crack length (m). The results of the indentation tests are plotted in Fig. 17. The slope of the curve is $P/C^{3/2} = 19.3$ MN m$^{-3/2}$. The hardness and elastic modulus of Y_2O_3 coatings on sapphire were previously found to be 8 and 150 GPa, respectively. The coating fracture toughness is calculated to be $K_c = 1.58$ MN m$^{-3/2}$. This value is approximately one-half that of bulk Y_2O_3 [20].

3.3.2. Interfacial fracture toughness, $K_{c,i}$

The Nanoindenter® was used to assess adhesion of Y_2O_3 coatings on sapphire. Six indentations were performed at depths ranging from 0.3–0.7 μm. However, the coating did not delaminate at indentation depths < 0.4 μm. Fig. 18a shows a typical load–displacement curve for a 0.67 μm indentation, in which the delamination event is characterized by an abrupt change in slope near zero load. The maximum indentor load, P, is plotted against crack length, C (Fig. 18b). The interfacial fracture toughness is

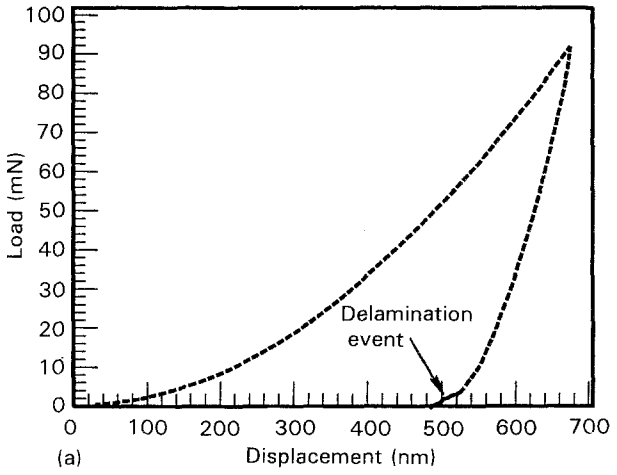

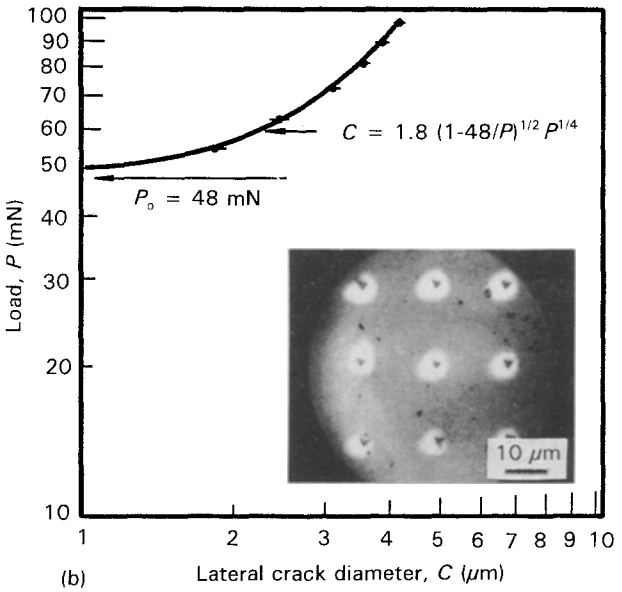

Figure 18 (a) Typical load–displacement curve produced using the Nanoindenter®. The coating delamination event is characterized by the change in slope near zero load. (b) Plot of Nanoindenter® load versus crack length use to determine Y_2O_3/Al_2O_3 interfacial toughness and light micrograph of several indentations (inset). Bright areas around indentations are indicative of debonding.

obtained from Equation 3, where $k = 0.16$, $t = 1 \times 10^{-6}$ m, $H_v = 8$ GPa, $P_0 = 48$ mN, $P = 75 \times 10^{-9}$ MN, and $C = 3 \times 10^{-6}$ m, and calculated to be $K_{c,i} = 0.15$ MN m$^{-3/2}$. This indicates that the Y_2O_3/Al_2O_3 interface is very weak.

3.3.3. Specific fracture energy, Γ_i

The specific fracture energy of the Y_2O_3 coating on sapphire is calculated using Equation 6, where the geometric crack factor $Y = \pi^{1/2}$ and the elastic modulus of the coating is $E = 150$ GPa. The specific fracture energy of the Y_2O_3 coating is $\Gamma_i = 4.7$ J m^{-2}. For $K_{c,i} = 0.15$ MN m$^{-3/2}$, the specific fracture energy of the Y_2O_3/Al_2O_3 interface is $\Gamma_i = 0.046$ J m^{-2}.

3.4. Y_2O_3 coating on polycrystalline niobium

3.4.1. Coating fracture toughness K_c

The fracture toughness of as-sputtered Y_2O_3 on

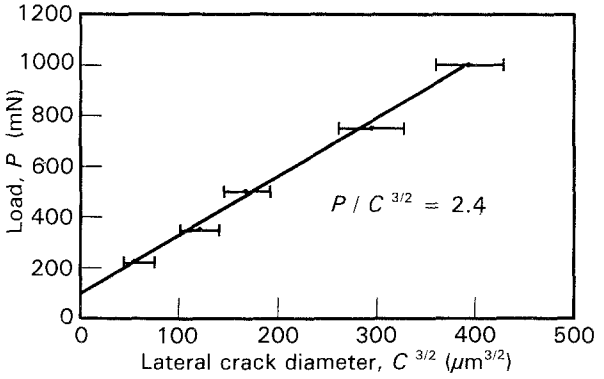

Figure 19 Plot of Vickers indentation load versus radial crack length used to determine the fracture toughness of sputtered Y_2O_3 coatings on niobium.

niobium was determined using Vickers indentation tests at loads ranging from 0.1–1 N. Y_2O_3 coatings on niobium did not exhibit a tendency to spall, unlike that found for Y_2O_3 coatings on Al_2O_3, and were thus not coated with gold. The indentor load, P, is plotted against crack length, $C^{3/2}$, and is shown in Fig. 19. The coating fracture toughness is calculated using Equation 7, where $P/C^{3/2} = 2.4$ MN m$^{-3/2}$, Vickers microhardness of Y_2O_3 is $H_v = 8$ GPa, coating elastic modulus $E = 150$ GPa, and found to be $K_c = 0.20$ MN m$^{-3/2}$. This value is approximately one-tenth of that found for Y_2O_3-coated Al_2O_3. The differences in fracture toughness are likely due to extensive deformation of the niobium substrate (Fig. 20) [10].

3.4.2 Interfacial fracture toughness, $K_{c,i}$

As-deposited Y_2O_3 coatings were not observed to debond from the niobium substrate at loads up to 0.078 N using the Nanoindenter® and 9.8 N using the Vickers indentor. However, lateral cracks formed in the Y_2O_3 coating at loads > 0.078 N (Fig. 20a and b). In contrast, as-sputtered Y_2O_3 coatings (with no gold overcoat) were observed to debond from Al_2O_3 at loads as low as 0.147 N. This result implies that the fracture toughness of the Y_2O_3/Nb interface is greater than the Y_2O_3/Al_2O_3 interface, but is not consistent with previous results where the Y_2O_3/Nb interface was found to be weaker than Al_2O_3/Nb [1] or Y_2O_3/Al_2O_3 [2].

Examination of the indentations showed that the Y_2O_3 coating did not buckle or spall at loads up to 9.8 N (Fig. 20b). Instead, the cracked coating appears to be well-bonded to the niobium substrate. A plot of indentor load versus lateral crack diameter (Fig. 21) does not reveal an asymptotic load at which lateral cracks vanish (Fig. 18b). This suggests that cracks caused by indentation tests propagate towards the surface rather than initiate delamination at the interface.

3.4.3. Specific fracture energy, Γ_i

The specific fracture energy of as-sputtered Y_2O_3 coating on niobium is calculated using Equation 6,

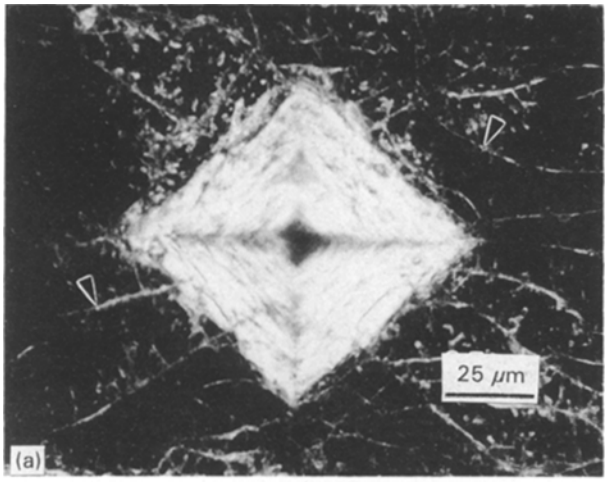

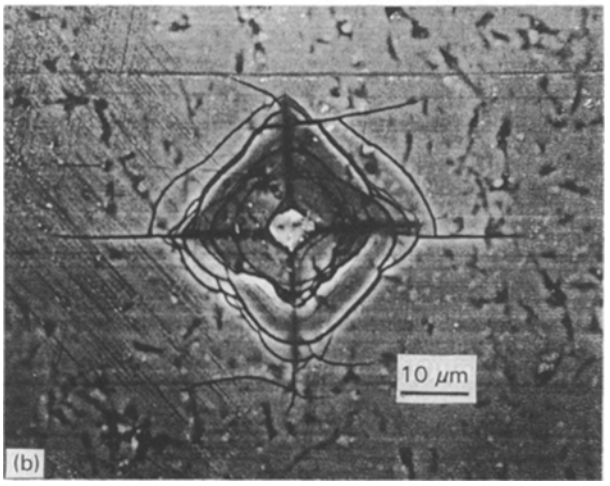

Figure 20 (a) Dark-field optical micrograph of a 9.8 N indentation for Y_2O_3-coated niobium. Note the numerous cracks emanating from the indentation. (b) Backscattered scanning electron micrograph of a 0.98 N indentation for Y_2O_3 coated niobium. Note the radial and lateral cracks, as well as adherence of the coating to the niobium substrate.

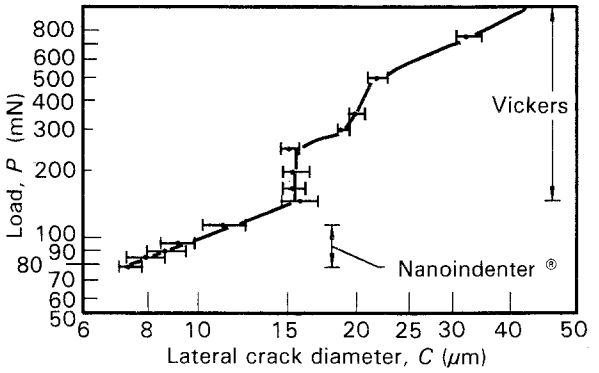

Figure 21 Plot showing the variation load versus lateral crack diameter for both Vickers ($P > 120$ mN) and Nanoindenter® ($P \lesssim 125$ mN) tests.

where $K_c = 0.2$ MN m$^{-3/2}$, $Y = \pi^{1/2}$, and $E = 150$ GPa. The specific fracture energy of the Y_2O_3 coating is $\Gamma_i = 0.074$ J m^{-2}.

3.5. Niobium coating on single-crystal Y_2O_3

3.5.1. Coating fracture toughness, K_c

The fracture toughness of as-sputtered niobium on Y_2O_3 was determined using Vickers indentation tests at loads ranging from 2–10 N. Niobium coatings did not exhibit a tendency to crack or spall at 2 N, while radial cracks were produced at 3, 5, and 10 N (Fig. 22). A plot of the indentor load, P, versus crack length, $C^{3/2}$, as measured from the niobium coating and transparent rearside of the Y_2O_3 wafer is shown in Fig. 23. The coating fracture toughness is calculated using Equation 7, where the average of the two curves is $P/C^{3/2} = 11.5$ MN m$^{-3/2}$, the Vickers microhardness of Y_2O_3 is $H_v = 2.8$ GPa, coating elastic modulus $E = 88$ GPa, and found to be $K_c = 1.22$ MN m$^{-3/2}$. This value is much lower than the room-temperature

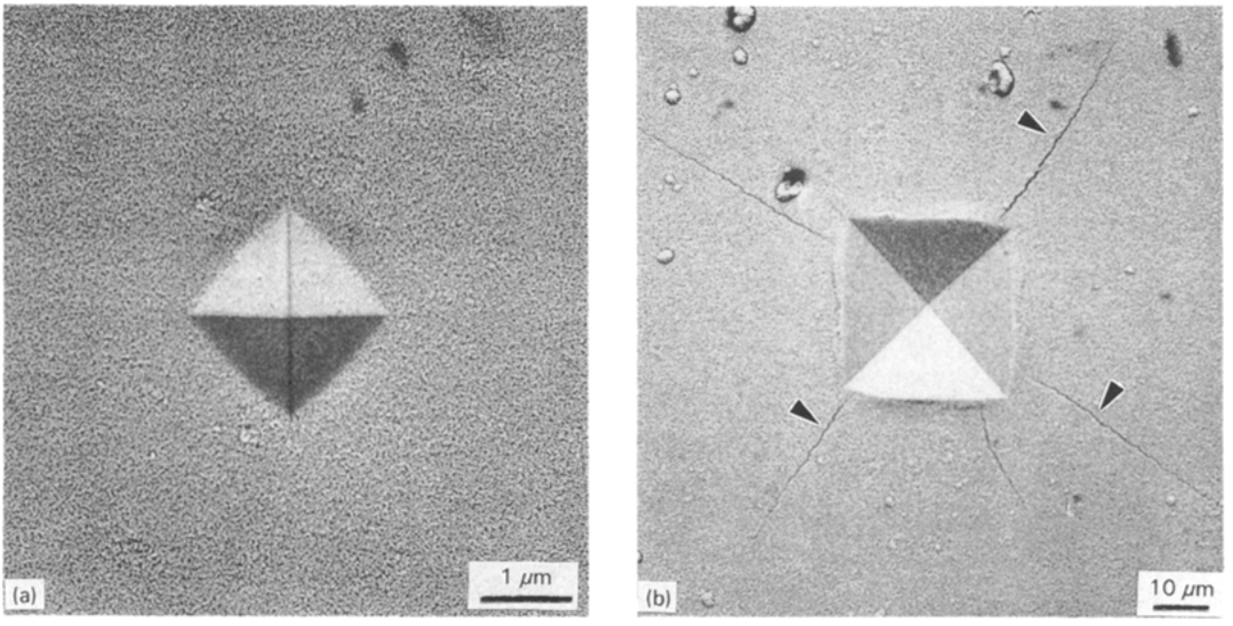

Figure 22 Scanning electron micrographs of indentations produced by loads of (a) 2 N and (b) 10 N showing radial cracks.

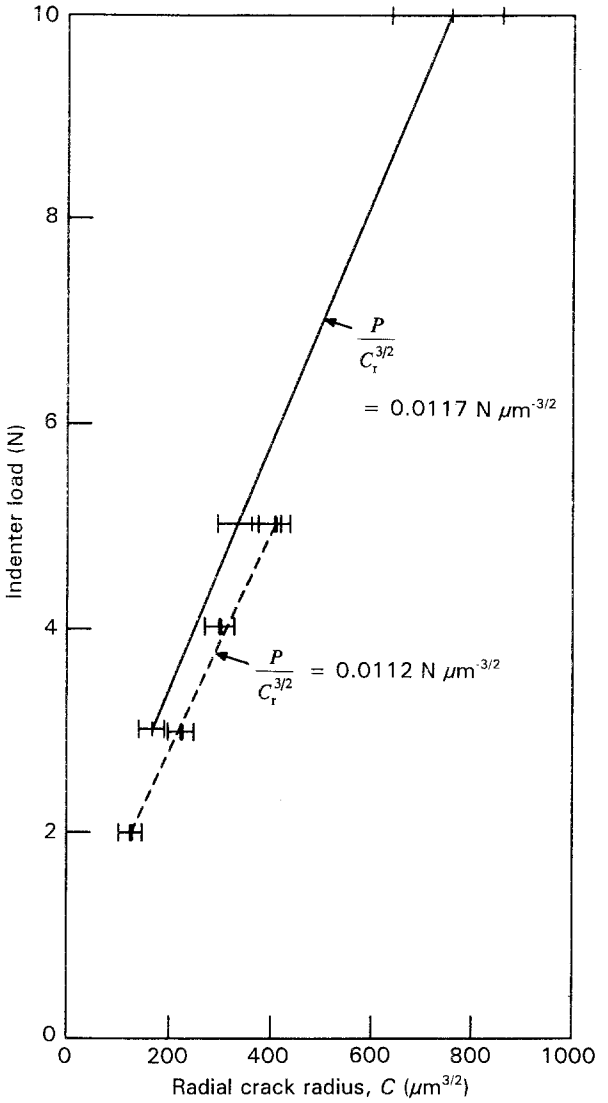

Figure 23 Plots of Vickers indentor load versus radial crack length for the niobium coating. Crack lengths were measured from the top (solid line, Fig. 22) and from the back through the transparent Y_2O_3 wafer, and show good correlation.

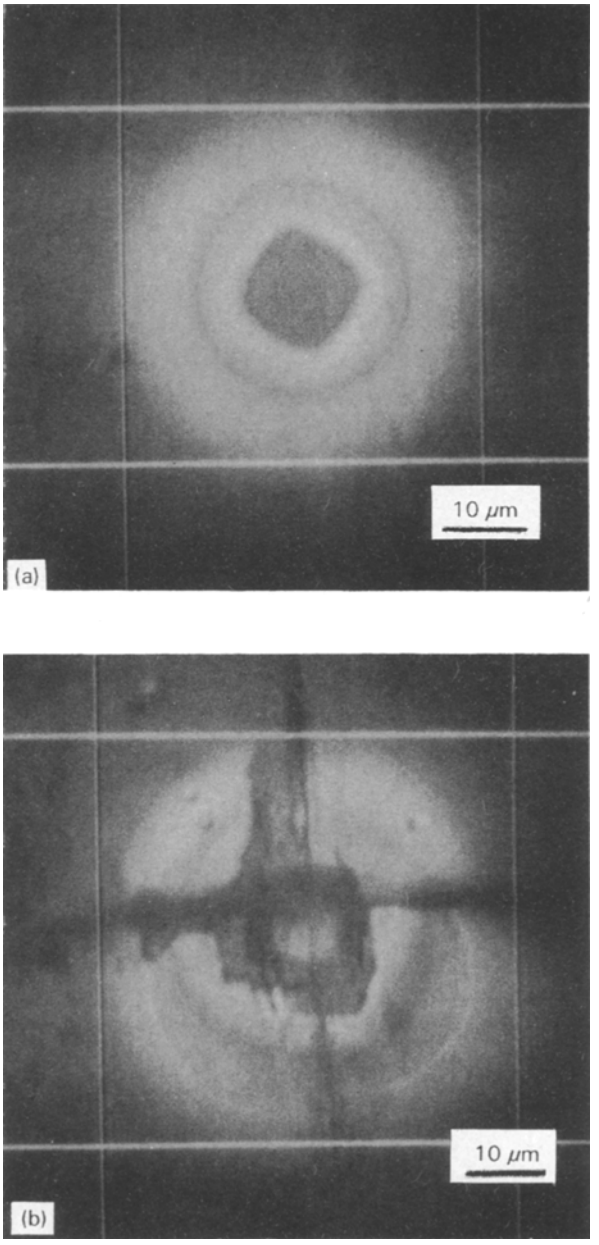

Figure 24 Light micrographs showing debonding of the niobium coating at loads of (a) 1.5 N and (b) 3 N, as viewed from the transparent rearside of the Y_2O_3 wafer. Radial cracks produced by the 3 N load are apparent.

fracture toughness of bulk niobium ([16] p. 363). The difference in fracture toughness is most likely due to coating thickness, columnar microstructure, and the presence of a residual stress in as-deposited niobium.

3.5.2. Interfacial fracture toughness, $K_{c,i}$

As-deposited niobium coatings were observed to debond from the Y_2O_3 substrate at loads as low as 0.25 N using the Vickers indentor. The delamination event was observed from the backside of the transparent Y_2O_3 substrate through the formation of interference rings (Fig. 24). A plot of indentor load, P, versus lateral crack length, C, is shown in Fig. 25. The interfacial fracture toughness is obtained from Equation 3, where $k = 0.16$, $t = 4 \times 10^{-6}$ m, $H_v = 2.8$ GPa, $P_0 = 135$ mN, $P = 1500$ mN, and $C = 20 \times 10^{-6}$ m, and calculated to be $K_{c,i} = 0.18$ MN m$^{-3/2}$. This value is two orders of magnitude lower than that measured in uniaxial tension tests of niobium-reinforced TiAl laminates with Y_2O_3 interfacial coating [6].

3.5.3. Specific fracture energy, Γ_i

The specific fracture energy of as-sputtered niobium on Y_2O_3 is calculated using Equation 6, where $K_c = 1.22$ MN m$^{-3/2}$, $Y = \pi^{1/2}$, and E(Nb) = 88 GPa. The specific fracture energy of the coating is $\Gamma_i = 4.78$ J m^{-2}. For $K_{c,i} = 0.18$ MN m$^{-3/2}$, the specific fracture energy of the Nb/Y_2O_3 interface is $\Gamma_i = 0.104$ J m^{-2}. The coating fracture toughness, interfacial fracture toughness, and specific fracture energy results presented in Sections 3.3–3.5 are summarized in Table I.

4. Discussion

4.1. Characterization of as-deposited Y_2O_3

Evaluation of reactively sputtered Y_2O_3 coatings

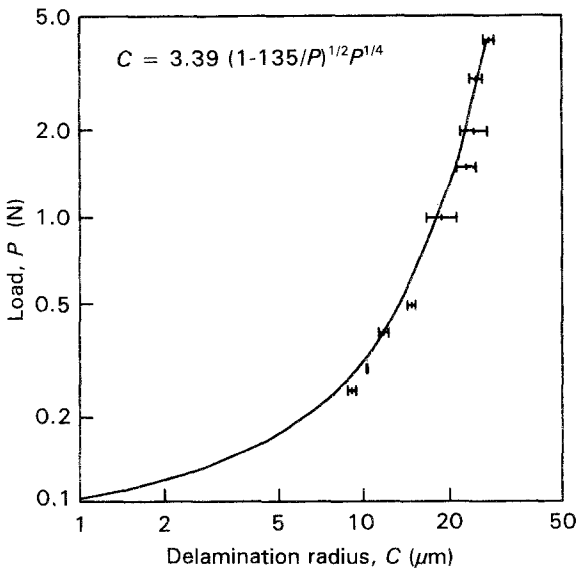

Figure 25 Plot of load versus crack length used to determine Nb/Y_2O_3 interfacial fracture toughness.

shows they are stoichiometric and contain low levels of impurities. The coating microstructure is typical of that found in thin vapour-deposited coatings examined through-thickness. A feature unique to vapour deposition is the range of microstructures, and hence physical and mechanical properties, that can be obtained in as-deposited coatings. An experimentally determined model of the structure of metal and ceramic coatings deposited by d.c. and r.f. sputtering as a function of working gas pressure and homologous temperature T/T_M, shows a trend from high aspect ratio columnar (Zone 1) to equiaxed (Zone 3) grains [18]. The Zone 1 microstructure consists of tapered crystallites with a fibrous internal structure, continuous voids at grain boundaries, and domed tops whose diameter increases with increasing substrate temperature. The formation of an intergranular network of voids is further enhanced by shadowing due to substrate surface roughness or preferential growth of crystallites and low adatom surface mobility. The mechanism by which grain boundaries coalesce to produce dense columnar microstructures is attributed to increased adatom mobility caused by higher T/T_M as well as increased desorption of inert gas atoms.

Coating microstructures produced at low T/T_M are found in most vapour-deposited coatings. Fig. 4 shows that sputtered Y_2O_3 coatings consist of columnar grains whose length extends through the entire coating thickness. These microstructures may be the least desirable because pipe diffusion can occur easily along porous grain boundaries and result in increased interaction with the substrate during hot pressing. In addition, sputtered coatings often contain a large amount of interfacial area which should affect the thermochemical stability and mechanical properties of the matrix/reinforcement interface [27–31]. The microstructure normally found in coatings deposited at low T/T_M may contain 50–400 grains/μm^2, resulting in 15%–25% grain-boundary area [27, 28, 30, 31] compared to 0.05% for bulk polycrystalline materials [27]. Coatings may contain additional interfacial area in the form of twins and stacking faults [29]. However, diffusion bonding niobium-reinforced TiAl results in a coating with better defined columnar grains, minimal reaction with the matrix or reinforcement, and composites with improved interfacial debonding and fracture toughness. This is due to the intrinsic thermochemical stability of Y_2O_3 in contact with niobium and TiAl, and thermodynamic preference to reduce interfacial area at the temperature and time used to bond the laminates together.

4.2. Nb/Al_2O_3 and Ti/Al_2O_3 interfaces

Uniaxial tension tests of precracked TiAl/Nb laminates fractured *in situ* in the scanning electron microscope showed that debonding occurs along the Nb/Y_2O_3 interface, which permits plastic deformation of the ductile phase over long lengths [6]. The yttria coating results in a 200% increase in work of fracture compared to Al_2O_3-coated niobium. The Nb/Y_2O_3 system has not been previously studied. However, both the Nb/Al_2O_3 [9, 32, 33] and Ti/Al_2O_3 [34–36] interfaces are well-characterized, and represent examples of non-reactive and reactive metal/ceramic systems, respectively. Understanding each provides a basis for determining the cause of a high work of rupture in Y_2O_3-coated niobium-reinforced TiAl.

The Nb/Al_2O_3 interface has been characterized by direct imaging using high-resolution TEM [9]. Pol-

TABLE I Summary of coating fracture data

Coating/substrate	Test method	K_c (MN m$^{-3/2}$)	$K_{c,i}$ (MN m$^{-3/2}$)	Γ_i (J m^{-2})
Y_2O_3/Al_2O_3	Indentation	1.58	–	4.70
Y_2O_3/Al_2O_3 interface	Indentation	–	0.15	0.046
Y_2O_3/Al_2O_3 interface [7]	Cone crack	–	3.65[a]	25
Y_2O_3/Nb	Indentation	0.20	–	0.074
Y_2O_3/Nb interface	Indentation	–	–	–
Y_2O_3/Nb interface [6]	Tensile	–	3.65[a]	25
Nb/Y_2O_3	Indentation	1.22	–	4.78
Nb/Y_2O_3 interface	Indentation	–	0.180	0.104
Y_2O_3/Nb interface [6].	Tensile	–	3.65[a]	25
Bulk Y_2O_3 [20]	Indentation	2.85	–	15

[a] $K_{c,i}$ obtained from Γ_i using Equation 6.

ished single crystals of niobium and Al_2O_3 were diffusion bonded at 1700 °C for 2 h in high vacuum ($\sim 10^{-3}$ Pa) and 10 MPa load. The couples were bonded in a $(1\,1\,0)_{Nb} \parallel (0\,0\,0\,1)_{Al_2O_3}$ and $[0\,0\,1]_{Nb} \parallel [2\,1\,1\,0]_{Al_2O_3}$ orientation relationship. Samples for high-resolution TEM were obtained from the bulk couple with foil planes normal to $[0\,0\,1]_{Nb}$ and $[1\,1\,0]_{Nb}$. High-resolution TEM of the interface did not reveal the presence of a reaction layer. This is in contrast to other studies, where niobium oxides [37] or impurities present in polycrystalline Al_2O_3 or niobium segregated or catalysed reactions at the interface during hot pressing [38]. Non-equilibrium phases may form at the interface due to diffusion of impurities to accommodate misfit strain. While Al_2O_3 is dissolved by niobium at $\sim$ 1700 °C, no metallic aluminium found in single-crystal couples bonded at 1700 °C for 2 h [9]. It is possible that a small amount of Al_2O_3 was dissolved and subsequently precipitated at the interface upon cooling. This should form defects at the interface due to the misfit strains developed at the interface, but none were observed. These results indicate that chemical interaction between high-purity single-crystal niobium and Al_2O_3 is minimal during diffusion bonding.

Another study examined the Nb/Al_2O_3 interface by internally oxidizing an Nb–3 at % Al alloy at 1450 °C [32]. No interfacial compounds were detected by high-resolution TEM, and the interface was observed to be atomically flat. The outer layer of Al_2O_3 was suggested to consist of a monolayer of oxygen atoms. The Nb/Al_2O_3 interface has also been examined by XPS and Auger electron spectroscopy (AES). Several monolayers of niobium were evaporated *in situ* on to (0 0 0 1) sapphire substrates heated to 1000 °C [33]. High-resolution spectra of Nb (3d), O(1s), and Al(2p) versus niobium coating thickness indicate that the niobium donates electrons to surface oxygen atoms to form Nb–O bonds. Thus, a chemical reaction occurs between niobium and Al_2O_3, but it is limited to approximately one monolayer.

The former TEM study [9] did not discuss the presence of an oxide layer on polished niobium (1–2 nm thick) or physisorbed or chemisorbed species on niobium or sapphire. Physisorbed species such as H_2O will mostly desorb upon heating, while monolayer coverage of hydrocarbon should innocuously diffuse into an infinite sink of niobium. At temperatures typical of diffusion bonding, the oxide layer on niobium will likely be reduced by bulk niobium, which has $\sim$ 0.1 wt % solubility for oxygen at 25 °C. Remarkably, efforts to determine the nature of the Nb/Al_2O_3 interface exhibit similar results while utilizing samples prepared by greatly different methods and with different levels of surface contamination [9, 32, 33].

The Ti/Al_2O_3 system, in contrast, is highly reactive, resulting in considerable degradation of the interface [34–36]. Single-crystal Al_2O_3 fibres, $\sim$ 300 μm diameter, were hot pressed between commercially pure α-titanium sheets $\sim$ 400 μm thick at 815 °C for 2 h and 110 MPa [34], then vacuum annealed at 600–1000 °C for times sufficient to produce measurable reaction zones and determine rate constants. The resulting reactions were characterized by XRD and electron microprobe. The reaction product after exposure to 1000 °C for 100 h was $\sim$ 40 μm thick and found to consist of Ti_3Al and TiAl. Microhardness measurements were used to determine the extent of oxygen diffusion into the surrounding matrix.

Reactions between thin films of titanium on bulk alumina and on alumina-containing substrates have been extensively studied [35, 36]. Single-crystal alumina substrates maintained at 25 and 1000 °C were coated with titanium by evaporation, then examined by XPS [35]. At 25 °C, several monolayers of titanium were found to reduce the Al_2O_3 surface and produce Ti–O bonds. In contrast, coatings deposited on substrates held at 1000 °C produced both Ti–O and Ti–Al bonds. In the former, titanium bonds to a monolayer of oxygen atoms on the oxide surface, while in the latter reduction of the oxide is extensive and enables the formation of titanium–aluminium compounds.

Interfacial reactions between titanium and amorphous cordierite-based ($2MgO \cdot Al_2O_3 \cdot 5SiO_2$) ceramic films 200 nm thick on single-crystal silicon were characterized by XPS [36]. Si–O bonds were found to dissociate at room temperature with sub-monolayer coverages of titanium. Additional coverage by titanium began to reduce Al–O bonds. Vacuum annealing results in increased reaction kinetics between titanium and SiO_2 and Al_2O_3. However, titanium was not observed to reduce the Mg–O bond up to 800 °C. Magnesium oxide-based compounds may be debond coatings worth investigating in titanium matrix composites.

It is apparent that a reactive system such as Ti/Al_2O_3 produces intermetallic reaction products that thicken with extended exposure to elevated temperature, thereby forming a more complicated interface. If the fracture energy of the reaction products is sufficient to discourage extensive debonding, then the toughness of the composite is reduced. For example, uncoated niobium plates diffusion bonded to TiAl reacted to form σ and T_2 phases 4–6 μm thick [6]. Tensile testing showed debonding occurred in the σ phase, which had a measured fracture energy of $\Gamma_i = 45\ J\ m^{-2}$. This is sufficient to retard debonding and reduce the work of rupture by 66%. These results suggest that there may be similarity between the Nb/Al_2O_3 and Nb/Y_2O_3 systems [6, 9, 32, 33]. The Nb/Y_2O_3 interface may be atomically sharp, similar to that found in Nb/Al_2O_3 [9]. This, coupled with a lower Y_2O_3 fracture energy, may cause the improved debonding and higher fracture toughness observed experimentally [6].

4.3. Relationships to debonding

The success of a particular material as a debond coating will depend on a combination of several factors, including coating thickness, surface and bulk impurities, local stress state, coating mechanical properties, bond strength between the coating and reinforcement or matrix, thermodynamic stability, and microstructure.

Coating thickness has not yet been quantified, but it is reasonable to assume that there are optimum thicknesses that may be defined by other variables in the composite system such as reinforcement size or diffusivity. Impurities in the bulk can accumulate at the interface [9], and are expected to be detrimental in most cases. The effect of surface impurities remains uncertain, but does not appear to cause difficulties in the case of Nb/Al_2O_3 [9, 32, 33]. However, the use of high surface area reinforcements such as multifilament fibre tows, whiskers, or particulates, may require preferential treatment to avoid the introduction of large amounts of physisorbed species. Interstitials or minor alloying elements may locally stabilize unwanted phases or precipitate new phases, thereby deleteriously affecting matrix properties.

Debonding has been observed in many fibre coating/matrix systems including $Nb/Y_2O_3/TiAl$ [6], $Al_2O_3/Mo/Al_2O_3$ [7], Al_2O_3/porous ZrO_2/Al_2O_3 [8]. SiC/C/AS [2], SiC/BN/SiC [39], and $W/Al_2O_3/TiTaAl_2$ [40]. The coefficient of thermal expansion (CTE) should be an important consideration in selecting debond coatings. In particular, the difference in relative CTE between the fibre/coating/matrix should be small ($\Delta\alpha$ = 1–3 p.p.m. $°C^{-1}$). In some case the interface is in compression, while in others the interface is in a small amount of tension. There seems to be no simple rule for determining which case is most desirable, other than that the magnitude of the tensile stress cannot be high.

Oxide coatings perform well in ductile phase-reinforced brittle-matrix systems because they fracture at low applied stress, enabling plastic deformation of the toughening phase [6]. The specific fracture energy, Γ_i, of oxide coatings is small, typically on the order of 25 J m^{-2}. The improved debonding obtained with Y_2O_3 versus Al_2O_3 coatings suggests the fracture energy of the former is lower. In addition, pores in the coating will affect coating fracture toughness and debonding behaviour of composites [8]. Thus, prior knowledge of thin-film fracture toughness, its dependence upon porosity, and control of porosity in the application of coatings can be useful in guiding future coating selection. Successful debond coatings must also be thermally stable and substantially non-reactive with respect to both the matrix and reinforcing phase. The Gibb's free energy of formation of α-Al_2O_3 and Y_2O_3 is -378.2 and -434.2 kcal mol^{-1}, respectively [41]. Yttria should, therefore, be more difficult to reduce by niobium and TiAl at typical diffusion-bonding temperatures and times, thus retaining a sharp interface. For similar reasons, Y_2O_3 also serves as a protective coating between the niobium reinforcement and the TiAl matrix.

The microstructure of sputtered Y_2O_3 was found to consist of tapered crystallites extending through the thickness of the coating, perhaps resulting in pipe diffusion and increased reaction with the matrix or reinforcement. Such interaction should affect debonding by altering the interfacial chemistry. While this may occur in some systems, it has not yet been observed in the composite system under investigation. Further, sputtered Y_2O_3 coatings evaluated in niobium-reinforced TiAl matrices remain columnar after hot-pressing (Fig. 8). Conversely, molybdenum and ZrO_2 coatings in Al_2O_3/Al_2O_3 laminate specimens become equiaxed after hot-pressing [7, 8]. This will also probably affect the mechanical properties of the coating, interface, or crack path. For example, thermal exposure during composite processing or coating microstructure may determine the location of debonding, i.e. within the coating, at the coating/fibre interface, or at the coating/matrix interface, whichever has the lowest specific fracture energy. No rationale has yet been developed to guide selection of the preferred debonding site.

4.4 Analysis of indentation-derived coating fracture results

4.4.1. Y_2O_3 coatings on Al_2O_3

The specific fracture energy of interfaces modified with coatings was measured by Hertzian cone cracking experiments using a model single-crystal Al_2O_3/Al_2O_3 composite system [7, 8]. The coatings evaluated include molybdenum, yttria-stabilized ZrO_2 (tetragonal structure), TiAl, m-ZrO_2 (m = monoclinic), and Y_2O_3. All coatings were deposited by sputtering, while the latter two were also applied using sol–gels, at a nominal coating thickness of 1 μm. Single-ply laminate specimens were fabricated by diffusion-bonding coated Al_2O_3 wafers in vacuum at 1000–1400 °C under a pressure of 1 MPa. Cracks were introduced into the Al_2O_3 laminate by applying a point load using a 12.5 mm WC ball. The Hertzian crack reaches the interface and either passes through the coating or is deflected by fracture along the interfacial coating, resulting in improved toughness. Coatings which exhibited this behaviour had low specific fracture energies and include molybdenum (Γ_i = 3–5 J m^{-2}) and ~ 50% porous monoclinic ZrO_2 (Γ_i = 4 J m^{-2}). Conversely neither sputtered nor sol–gel Y_2O_3 coatings were suitable because they reacted partially with the Al_2O_3 substrate to form YAG at the interface, resulting in a high specific fracture energy (Γ_i = 25 J m^{-2}).

The fracture toughness and specific fracture energy of the Al_2O_3/Y_2O_3 interface measured in the present study by indentation tests are 0.15 MN $m^{-3/2}$ and 0.046 J m^{-2}, respectively (Table I). Both values are lower than expected. The difference is attributed to the evaluation of as-deposited coatings which did not react with the Al_2O_3 substrate to form YAG, due to the low substrate temperature during sputtering, and the columnar microstructure. The low specific fracture energy of the Y_2O_3/Al_2O_3 interface (Γ_i = 0.046 J m^{-2}) is indicative of weak bonding between as-deposited Y_2O_3 coating and the alumina substrate.

4.4.2. Y_2O_3 coatings on niobium

The interfacial debonding characteristics of sputtered Al_2O_3 and Y_2O_3 interface in a TiAl/Nb composite showed that the preferred debond coating is Y_2O_3. The specific fracture energy of the Y_2O_3/Nb interface

is $\sim 25\ J\ m^{-2}$, and is sufficiently low in this composite system to promote extensive plastic deformation of the ductile phase over a large volume. Debonding, coupled with a ductile phase which easily work hardens, results in a composite with high toughness. Indentation test data (Table I) show that the calculated fracture toughness and fracture energy of as-deposited Y_2O_3 on niobium reflect failure of the Y_2O_3 coating and deformation of the niobium substrate as a single unit. Thus, measurements of $K_{c,i}$ could not be made because coating failure is not independent of the substrate.

4.4.3. Niobium coatings on Y_2O_3

Indentation tests to determine the fracture toughness and fracture energy of the Nb–Y_2O_3 interface could not only be assessed if the test specimen geometry were reversed, i.e. sputtered niobium coating on single-crystal Y_2O_3. The interfacial fracture toughness is an order of magnitude lower than that found in uniaxial tensile tests of niobium-reinforced TiAl laminates [6]. As a result, the specific fracture energy of the Nb–Y_2O_3 interface as determined by indentation tests did not correlate with that found in tensile tests using diffusion-bonded Nb–TiAl laminates.

4.4.4. Bulk Y_2O_3

The fracture toughness of bulk Y_2O_3 reportedly varies from $2.3–3.4\ MN\ m^{-3/2}$ [20], resulting in $\Gamma_i = 9.95–21.7\ J\ m^{-2}$. Conversely, the measured indentation-derived fractured toughness of as-deposited Y_2O_3 coating on sapphire is $1.58\ MN\ m^{-3/2}$, resulting in $\Gamma_i = 4.7\ J\ m^{-2}$ (Table I). The intrinsic fracture toughness of as-deposited Y_2O_3 coating is about half that of bulk Y_2O_3. The difference is due to the evaluation of dissimilar microstructures, i.e. sub-micrometre columnar Y_2O_3 grains for vapour-deposited Y_2O_3 versus equiaxed grains in bulk Y_2O_3. Regardless, reasonable correlation to bulk properties can be achieved via Vickers indentation testing, provided the coating is deposited on to a hard substrate.

4.5. Factors affecting fracture toughness results

There are several factors which can affect the response of the coating to indentation tests. These include thickness, residual stress, bond strength, microstructure, and elastic modulus. The hardness, elastic modulus, and fracture properties of micrometre-thick coatings can be evaluated using the Nanoindenter®. However, the loads required to initiate radial cracks at the corners of the indentation may exceed that load range of this instrument, as was the case for as-deposited Y_2O_3 coatings on sapphire (Section 3.3.1). Thus, it is reasonable to assume that there is minimum thickness that is required for testing. The present study indicates that coatings $\sim 1\ \mu m$ thick are suitable for testing. This is also a useful coating thickness for applications requiring debond coatings on monofilament or multifilament fibres.

Residual tensile or compressive stresses are commonly found in as-deposited sputtered coatings, and may be caused by the sputtering equipment geometry or deposition conditions. These include target-to-substrate distance, working gas pressure, reactive gas partial pressure, substrate bias, or coating/substrate thermal expansion mismatch [42]. The residual stress in as-deposited films can affect indentation tests. For example, coatings with residual compressive stress may inhibit radial cracking and result in higher K_c. Conversely, $K_{c,i}$ may be reduced due to a propensity for the coating to buckle. Residual stress may not be a significant factor in the present study because the fracture toughness of as-deposited Y_2O_3 is in reasonable agreement with bulk Y_2O_3.

The bond between the coating and substrate must have sufficient strength to allow the coating to be probed at loads required to produce the desired coating fracture morphology. This will be most greatly influenced by post-deposition processing of the coating/substrate system such as hot-pressing. Laminate samples previously evaluated were hot-pressed at temperatures ranging from 1066–1450 °C [6, 7], which may result in the formation of interfacial compounds. For example, Y_2O_3 coatings on sapphire reacted to form a layer of YAG at the interface [7]. The interfacial fracture toughness of this system will be higher than as-sputtered Y_2O_3 on sapphire.

The microstructure of as-deposited Y_2O_3 coatings consists of tapered crystallites extending through the thickness of the coating and is produced by low adatom mobility due to low homologous temperature and preferential growth of crystallites [18]. This microstructure will affect the results of indentation tests because the load is applied parallel to columnar grains. The difference in fracture toughness between as-deposited Y_2O_3 and bulk Y_2O_3 is attributed to evaluation of dissimilar microstructures, i.e. sub-micrometre columnar Y_2O_3 grains for vapour-deposited Y_2O_3 versus 1–10 μm diameter equiaxed grains in bulk Y_2O_3 [20].

Calculations to determine Γ_i utilize the elastic modulus of Y_2O_3 as determined by the Nanoindenter®. This value, 150 GPa, agrees with that previously determined for bulk Y_2O_3 [23]. The elastic modulus is determined by a uniaxial tension test where stress is linearly proportional to strain. However, this condition is not satisfied by indentation tests nor for thin coatings attached to a substrate. In addition, the indentor does not load the coating in uniaxial tension, the condition under which Young's modulus is obtained. The elastic modulus is also a directional property [43], so the modulus of free-standing films deposited at low T/T_M will be anisotropic and vary depending upon orientation to the columnar grains. These factors cause uncertainty in the application of bulk elastic properties to the determination of K_c and Γ_i.

The modulus of elasticity is also a function of the type of chemical bonding in a crystal, i.e. ionic, covalent, metallic [43]. A thin free-standing film should, therefore, exhibit bulk elastic properties, provided the ratio of surface atoms to interior atoms is low. A 1 μm

thick film contains ~ 3000 atoms through-thickness, which should be sufficient to satisfy this criterion and exhibit bulk or near-bulk properties. A similar argument may also apply to other properties of coatings 1–2 μm thick.

The elastic modulus of supported and unsupported thin films has been determined by different techniques, and varies from 0.1–0.9 of bulk properties [45–46]. These results indicate that elastic properties are dependent upon many variables related to mechanical test conditions, coating deposition method, and perhaps even sputter-deposition parameters. The specific fracture energy of as-deposited Y_2O_3 on Al_2O_3 was found to be 4.7 J m^{-2} (Table I). Calculation of this parameter using 75 and 15 GPa (instead of 150 GPa) yields specific fracture toughnesses of 9.4 and 46.9 J m^{-2}, respectively. The specific fracture energy of as-deposited Y_2O_3 approaches that of bulk Y_2O_3 for $E = 75$ GPa. However, there are distinct differences in microstructure as previously noted. Thus, values of K_c and $K_{c,i}$ calculated for as-deposited Y_2O_3 on sapphire using Young's modulus for bulk Y_2O_3 may, indeed, be indicative of actual coating fracture properties and interfacial debonding behaviour.

The calculated values for fracture toughness and fracture energy derived by indentation tests must be used carefully because numerous test-related factors can affect the results [13, 14, 19, 47]. Many of the factors related to the coating, its deposition, or indentation test technique are difficult, if not impossible to control. However, the results presented in Table I show that indentation and tests can be used to determine coating fracture properties, K_c, with reasonable correlation to bulk properties. However, the interfacial fracture toughness, $K_{c,i}$, and specific fracture energy, Γ_i, could not be correlated to results obtained from laminates evaluated by tensile [6] or cone crack [7, 8] tests. This is attributed to differences in test methods and sample preparation. For example, tensile tests to determine Γ_i in niobium-reinforced TiAl measures decohesion along two interfaces, while indentation tests measure only one interface. Hertzian cone crack tests are an elastic indentation test method, while Nanoindenter® and Vickers indentation tests are plastic indentation test methods. Samples prepared by r.f. sputtering were not exposed to the same thermal history as diffusion-bonded samples.

5. Conclusion

The fracture toughness, interfacial fracture toughness, and specific fracture energy for as-sputtered Y_2O_3 coatings on sapphire and commercial purity polycrystalline niobium substrates, and niobium-coated Y_2O_3 were determined via micro- and nanoindentation techniques. The results were compared to fracture toughness studies of Al_2O_3/Al_2O_3 [7, 8] and niobium-reinforced TiAl laminate coupons containing Y_2O_3 interfacial coating [6]. The calculated fracture toughness of as-deposited Y_2O_3 on sapphire was similar to reported values for bulk Y_2O_3. However, the fracture toughness of the Y_2O_3-Nb interface is lower than that previously reported. As a result, the specific fracture energy of the interface was also lower than expected, and is attributed to differences in coating microstructure and weak bonding between as-deposited coatings and the substrates.

These results were related to factors which may affect debonding and fracture toughness of brittle matrix composites. Reactive and non-reactive metal/ceramic systems were reviewed in an effort to understand why this coating performs well. It is postulated that Y_2O_3-coated niobium has an atomically sharp interface which has a lower fracture energy compared to Nb/Al_2O_3, resulting in improved debonding and fracture toughness in niobium-reinforced TiAl [6]. Additional studies must be performed to quantify better the attributes common to fibre/coating/matrix systems that exhibit desirable fracture behaviour, so that predictive guidelines can be used to select debond and protective coatings.

Acknowledgements

This work was funded by Defense Advanced Research Projects Agency and monitored by the Air Force Office of Scientific Research under contract number F49620-89-C-0066. The author gratefully acknowledges the valuable support for this work provided by W. Coblenz of DARPA, L. Schioler formerly of AFOSR, R. Hecht and J. Spence of Pratt and Whitney, M. Abouelleil, B. Laube, and D. Snow of United Technologies Research Center, and J. Davis and A.G. Evans of the University of California at Santa Barbara.

References

1. A. G. EVANS and D. B. MARSHALL, *Acta Metall.* **37** (1989) 2567.
2. H. C. CAO, E. BISCHOFF, O. SBAIZERO, M. RÜHLE, A. G. EVANS, D. B. MARSHALL and J. J. BRENNAN, *J. Am. Ceram. Soc.* **73** (1990) 1691.
3. V. GUPTA, A. S. ARGON and J. A. CORNIE, *J. Mater. Sci.* **24** (1989) 2031.
4. M. BASCHE, R. FANTI and F. GALASSO, *Fiber Sci. Technol.* **1** (1968) 19.
5. F. WAWNER, A. Y. TENG and S. R. NUTT, *SAMPE Q.* **14** (1983) 39.
6. H. DÈVE, A. G. EVANS, G. R. ODETTE, R. MEHRABIAN, M. L. EMILIANI and R. J. HECHT, *Acta Metall. Mater.* **38** (1990) 1491.
7. J. DAVIS, H. C. CAO, G. BAO and A. G. EVANS, *ibid.* **39** (1991) 1019.
8. A. G. EVANS, A. BARTLETT, J. B. DAVIS, B. D. FLINN, M. TURNER and I. E. REIMANIS, *Scripta Metall. Mater.* **25** (1991) 1003.
9. W. MADER and M. RÜHLE, *Acta Metall.* **37** (1989) 853.
10. L. G. ROSENFELD, J. E. RITTER and T. J. LARDNER, "Interfaces in Composites", Materials Research Society Symposium Proceedings, Vol. 170 (Materials Research Society, Pittsburgh, PA, 1990) p. 11–16.
11. T. B. MASSALSKI, (Ed.), "Binary Alloy Phase Diagrams", Vol. 2 (American Society for Metals, Metals Park, OH, 1986) p. 1799.
12. M. ABOUELLEIL, L. CONOPASK, W. NIGHAN, W. ROMAN and D. PRICE, *Ceram. Trans.* **15** (1990) 457.
13. C. B. PONTON and R. D. RAWLINGS, *Mater. Sci. Technol.* **5** (1989) 961.
14. *Idem, ibid.* **5** (1989) 865.

15. S. CHAING, D. MARSHALL and A. EVANS, in "Surfaces and Interface of Ceramics and Ceramic/Metal Systems", edited by J. Pask and A. Evans, (Plenum Press, New York, 1981) pp. 603–17.
16. R. W. HERTZBERG, "Deformation and Fracture Mechanics of Engineering Materials", (Wiley, New York, 1976) pp. 255–96.
17. B. A. MOVCHAN and A. V. DEMSHICHIN, *Phys. Met. Metall.* **28** (1969) 83.
18. J. A. THORNTON, *Ann. Rev. Mater. Sci.* **7** (1977) 239.
19. P. SARGENT, in "Microhardness Techniques in Materials Science and Engineering", edited by P. Blau and R. Lawn, ASTM STP 889 (American Society for Testing and Materials, Philadelphia, PA, 1986) pp. 160–74.
20. G. FANTOZZI, G. ORANGE, K. LIANG and E. GILLET, *J. Am. Ceram. Soc.* **72** (1989) 1562.
21. P. J. BURNETT and D. S. RICKERBY, *Thin Solid Films* **148** (1987) 51.
22. R. COOK, M. PASCUCCI, and H. RHODES, *J. Am. Ceram. Soc.* **73** (1990) 1873.
23. J. HAGGERTY, "Production of Fibers by a Floating Zone Fiber Drawing Technique", Final Report, NASA Report CR-120984, May 1972, p. 52.
24. H. BAKER (ed.), "Metals Handbook", Vol. 2, 9th Edn (ASM International, Metals Park, OH, 1979) p. 779.
25. *Idem*, Vol. 2, 10th Edn (ASM International, Metals Park, OH, 1990) pp. 567–68.
26. B. LAWN, A. EVANS and D. MARSHALL, *J. Am. Ceram. Soc.* **63** (1980) 574.
27. P. M. FABIS, *J. Vac. Sci. Technol.* **A5** (1987) 75.
28. M. EMILIANI, M. RICHMAN and R. BROWN, *J. Mater. Sci.* **25** (1990) 137.
29. *Idem, ibid.* **25** (1990) 144.
30. R. BIRRINGER, *Mater. Sci. Eng.* **A117** (1989) 33.
31. D. J. SROLOVITZ, *J. Vac. Sci. Technol. A* **6** (1986) 2925.
32. M. KUWABARA, J. C. H. SPENCE and M. RÜHLE, *J. Mater. Res.* **4** (1989) 972.
33. F. S. OHUCHI, *J. Mater. Sci. Lett.* **8** (1989) 1427.
34. J. KENNEDY and G. GESCHWIND, in "Titanium Science and Technology", Vol. 4, edited by R. I. Jaffee and H. M. Burte (Plenum Press, New York, 1973) p. 2299.
35. J. H. SELVERIAN, M. BORTZ, F. S. OHUCHI and M. R. NOTIS, in "Electronic Packaging Materials Science III", edited by R. Jaccodine, K. A. Jackson and R. C. Sundahl, Materials Research Society Symposium Proceedings, Vol. 108 (Materials Research Society, Pittsburgh, PA, 1988) p. 107.
36. M. BORTZ and F. S. OHUCHI, *J. Appl. Phys.* **64** (1988) 2054.
37. S. MOROZUMI, M. KIKUCHI and T. NISHINO, *J. Mater. Sci.* **16** (1981) 2137.
38. Y. ISHIDA, H. ICHINOSE, J. WANG and T. SUGA, in "Proceedings of the 46th Annual Meeting of EMSA", edited by G. W. Bailey (San Francisco Press Inc., San Francisco, CA, 1988) p. 728.
39. R. NASLAIN, O. DUGNE, A. GUETTE, J. SEVELY, C. R. BROSSE, J-P. ROCHER and J. COTTERET, *J. Am. Ceram. Soc.* **74** (1991) 2482.
40. H. E. DÈVE and M. J. MALONEY, *Acta Metall. Mater.* **39** (1991) 2275.
41. R. C. WEAST (Ed.), "CRC Handbook of Chemistry and Physics", 68th Edn (CRC, Boca Raton, FL, 1987) p. D-51 and D-92.
42. J. A. THORNTON, in "Deposition Technologies for Thin Films and Coatings", edited by R. F. Bunshah (Noyes, Park Ridge, NJ, 1982) pp. 170–243.
43. M. F. ASHBY and D. R. H. JONES, "Engineering Materials" (Pergamon Press, New York, 1980) Chs 3 and 4.
44. M. L. SCOTT, in "Laser-Induced Damage in Optical Materials", NBS Special Publication 688, November 1985.
45. R. W. HOFFMAN, in "Thin Films: Stresses and Mechanical Properties", Materials Research Society Symposium Proceedings, Vol. 130, edited by J. D. Bravman, W. D. Nix, D. M. Barnett and D. A. Smith (Materials Research Society, Pittsburgh, PA, 1989) p. 87–92.
46. T. P. WEIHS, S. HONG, J. C. BRAVMAN and W. D. NIX, *ibid.* p. 295–306.
47. J. D. HORNER, in "Testing of Metallic and Inorganic Coatings", edited by W. B. Harding and G. A. Bari, ASTM STP 947 (American Society for Testing and Materials, Philadelphia, PA, 1987) p. 96.

Received 31 March 1992
and accepted 24 February 1993